The International Archives of the Photogrammetry, Remote Sensing and Spatial Information Sciences, Volume XLIX-B1-2026
XXV ISPRS Congress 2026 "From Imagery to Understanding", Commission I, 4–11 July 2026, Toronto, Canada

Estimating laser scanner's effective laser beam footprint using line spread function

Omar AbdelGafar[1], Selin Palaz[1], Yihui Yang[1], Derik Lichti[2], Christoph Holst[1]

[1] Chair of Engineering Geodesy, TUM School of Engineering and Design, Technical University of Munich, Munich, Germany
{o.abdelgafar, yihui.yang, christoph.holst}@tum.de
[2] Department of Geomatics Engineering, University of Calgary, Calgary, Canada
ddlichti@ucalgary.ca

Keywords: TLS, Laser Beam, Laser footprint, Resolution capability, Point spread function, line spread function.

Abstract

Accurate characterization of the terrestrial laser scanner (TLS) beam footprint is essential for understanding the stochastic behavior of the scanner. Estimating the laser footprint is crucial for determining the correlation length between neighboring observations, and thus for providing a realistic estimation of the correlation elements within the variance-covariance matrix quantifying the measurement uncertainties. In this contribution, an intensity-based workflow is introduced to estimate the effective laser beam footprint by deriving the line spread function (LSF) from the edge spread function (ESF). This effective laser beam footprint depends on the dynamic surface response over the interaction region between the emitted laser beam and the surface. The proposed method applies no assumptions regarding the geometric or physical behavior of the beam, allowing the footprint to be determined directly from the measured intensity values. Using the BOTA8 target, the Z+F Imager 5016A was investigated at two different distances and two scanning rates with varying mirror rotation speeds. The results provide insights into the influence of distance and scanning rate on the effective laser beam footprint.

1. Motivation

Terrestrial laser scanners (TLS) are increasingly being used in geodetic engineering applications that require millimeter-level accuracy (Holst and Kuhlmann, 2016), particularly in the deformation monitoring of critical infrastructures such as water dams (Kerekes and Schwieger, 2021) and bridges (Zhou et al., 2024). Therefore, the estimation of TLS measurement uncertainties is essential to distinguish actual deformations from measurement noise (Yang and Holst, 2025).

To model the TLS measurement uncertainties, a fully propagated variance-covariance matrix (VCM) is constructed for the TLS polar observations, namely the range r, the horizontal angle φ, and the vertical angle θ. This matrix is intended to represent the combined influence of the error sources affecting these measurements, including scanner imperfections, atmospheric conditions, scanning geometry, and the physical properties of the scanned surface (Soudarissanane et al., 2011).

The diagonal elements of the VCM represent the variances of the TLS polar measurements for each point in the point cloud, while the off-diagonal elements describe the correlations between these observations. Most existing studies focus mainly on estimating the diagonal components, while the correlation terms are typically neglected and set to zero because of the limited knowledge of their actual values (Schmitz et al., 2021).

However, in TLS, each range measurement results from a weighted integral of the surface response over the interaction region between the emitted laser beam and the surface – this surface response, in the end, is also influenced by the laser scanning rate; hence, it is also depends on scanning dynamics. We refer to the area of this surface response as *effective laser beam footprint* in analogy to the effective number of measurements introduced for scanning by Schmitz et al. (2020). The overlap between neighboring effective footprints resulting from dense data acquisition introduces spatial correlations among adjacent points. Therefore, estimating the effective laser beam footprint is essential for quantifying the correlation components.

To estimate the laser beam footprint, several studies have approached the problem empirically, relying on laboratory experiments and direct observations of the beam–object interaction (Schmitz et al., 2020; Chaudhry et al., 2021). In these studies, test specimens were used to determine the footprint based on observed mixed-pixel effects in the transition areas (Lichti et al., 2005). In contrast, Lichti and Jamtsho (2006) applied optical transfer function (OTF) theory, which characterizes how spatial frequencies are transmitted through an optical system and defines the imaging quality of the laser beam.

Our study introduces a workflow to estimate the effective laser beam footprint from the spatial-domain perspective of the OTF theory by employing the line spread function (LSF) using the intensity values of the scanned target. This allows the investigation of factors such as the incidence angle that may influence the estimation of the effective laser beam footprint. Accordingly, this study aims to address the following research questions:

- How can the effective laser beam footprint be derived from the LSF in the spatial domain?
- Which measurement configuration is required to apply the proposed workflow?
- What is the characteristic shape of the effective laser beam footprint of the Z+F Imager 5016A?

This paper is structured as follows: Section 2 reviews related work, Section 3 presents the proposed workflow, Section 4 describes the experimental setup, Section 5 discusses the results, and Section 6 concludes the study.

2. Related works

In TLS, each range measurement results from an average over the interaction of the scanner laser beam with the surface, i.e., over the effective laser beam footprint, obtained by weighted integration of the reflected signal from the surface area covered by the beam (Chaudhry et al., 2021). This averaging process smooths fine geometric details and reduces edge sharpness.

Since the laser footprint typically ranges from millimeters to centimeters, adjacent footprints often overlap, introducing spatial correlations within the point cloud. Moreover, estimating the effective laser beam width in a certain direction enables quantifying how well the scanner can distinguish fine surface details by defining the resolution capability of the system in that direction (Barbarella et al., 2017; Pesci et al., 2011).

For simplification, some methods assume the laser footprint to be circular (Huxhagen et al., 2011). However, (Schäfer, 2017) demonstrated that the effective laser beam footprint is elliptical rather than circular. Hence, assuming a circular footprint implies isotropic behavior, which does not fully represent the anisotropic characteristics introduced by the optical configuration of the laser system, including asymmetric beam divergence and astigmatic effects caused by the interaction of the beam with mirrors and lenses. Therefore, estimating the laser beam is essential for understanding both the geometric and stochastic properties of TLS measurements (Schmitz et al., 2021). This motivated many studies to investigate the laser beam footprint, which are discussed in the following sections.

To empirically estimate the resolution capability of TLS, Schmitz et al. (2020) introduced a methodology based on a test specimen proposed by Böhler et al. (2003), referred to as the Böhler star. The specimen consists of two parallel planes, where the foreground plane has triangular recesses that increase in size from the center toward the edge, while the background plane is a solid surface. By analyzing the transition areas that occur when the laser beam hits both the foreground and the background, the transition length can be quantified as the minimum distance between the convex hull estimated on the foreground and that on the background. By estimating the transition distance at each of the recess edges, a single convex hull can be used to link the transition distances across all edges. Other studies, such as Chaudhry et al. (2021); Centeno et al. (2010); Wang et al. (2016), simplified the target geometry to form a single edge between two planes for estimating the beam footprint.

Alternatively, to describe the scanner's resolution capability, (Lichti and Jamtsho, 2006) modeled the laser beam by considering the OTF. By assuming a Gaussian beam, the beam radius was defined at the $1/e^2$ intensity level. This study also introduced the concept of the effective instantaneous field of view (EIFOV), derived from the beam width and the angular sampling interval, to quantify the scanner's ability to resolve small-scale surface features.

From all the mentioned studies, it can be observed that beam estimation is generally based on physical assumptions, either assuming that the beam follows a Gaussian distribution or that the footprint has predefined shapes, such as circular or elliptical. Moreover, these approaches rely on range measurements between the scanner and the target surface.

Based on this state of the art, our article introduces a method for determining the effective laser beam footprint, mainly based on the intensity values of the scanned target – instead of the range measurements. Furthermore, our developed methodology is able to identify the shape of the footprint so that non-elliptical shapes could also be identified – if existent. Hence, our strategy does not rely on any assumptions regarding the beam shape or its characteristics.

3. Methodology

To estimate the effective laser beam footprint based on the OTF theory, two approaches can be considered: in the frequency domain, by estimating the modulation transfer function (MTF), or in the spatial domain, from the viewpoint of the impulse response (Boreman, 2021). In the spatial domain, there are two methods for estimation, namely through the point spread function (PSF) or the line spread function (LSF), which will be illustrated in Section 3.1. By adopting the LSF approach, a workflow is introduced to estimate the beam footprint in the context of laser scanning, as described in Section 3.2.

3.1 From point spread function to line spread function

If an infinitesimal point in space is observed by an ideal optical system, it would appear as a single, perfectly sharp point. However, in reality, the system does not capture this point ideally. Since the system acquires the backscattered signal from a finite illuminated area, the point appears blurred rather than sharp, as shown in Figure 1 (left). In the case of a TLS, this blurring occurs due to the laser foot print and other several factors, including optical aberrations, diffraction within the optics, electronic filtering, and the limited temporal response of the receiver. However, the effect of these factors is very small compared to the dominant influence of the laser footprint, where the reflected energy is distributed over a finite footprint on the surface (Goodman, 2005; Boreman, 2021).

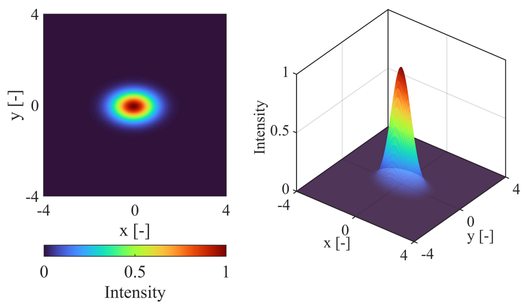

Figure 1. Image of a single point in the optical system space (left) and its corresponding PSF (right).

The size and shape of this footprint depend on the beam divergence, incidence angle, surface roughness and reflectivity (Barbarella et al., 2017; Chaudhry et al., 2021). Therefore, the recorded signal represents the integrated energy reflected from the illuminated area, referred to as the impulse response of the system $m(x, y)$, also known as the point spread function (PSF), where x and y are the spatial coordinates in the optical system, as illustrated in Figure 1 (right).

By estimating the PSF, the beam width can be determined using two conventions: the full width at half maximum (FWHM) and the $1/\mathrm{e}^2$ beam diameter, where e denotes Euler's number ($\mathrm{e} \approx 2.718$). However, estimating the PSF directly is challenging, as it requires an infinitesimal point target with high reflectivity and strong contrast against the background. Since realizing such a

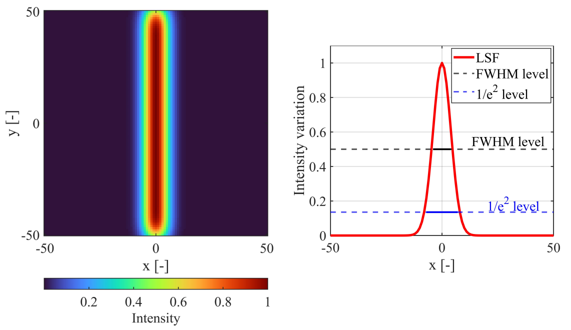

Figure 2. Image of a straight line along y-direction in the optical system space (left) and its corresponding LSF together with different representations of the beam width (right).

point target is difficult in practice, a more practical alternative is to consider the line spread function (LSF).

When a perfect line is observed by an optical system, the resulting image appears as a blurred line on both sides, as shown in Figure 2 (left). This blurring occurs because the line consists of an infinite number of infinitesimal points, each having a system response described by the PSF. As the blurring takes place in the direction orthogonal to the line, this response is distributed along this direction. By integrating all responses along the line direction, the cumulative intensity variation across the line can be obtained, representing the LSF (Williams, 1999), as illustrated in Figure 2 (right).

If the line is oriented along the y-direction, the LSF will be formed along the x-direction and can be expressed as

$$\mathrm{LSF}(x) = \int_{-\infty}^{+\infty} \mathrm{PSF}(x, y)\, dy. \tag{1}$$

For a single line in the object space, there will be one corresponding LSF that describes the intensity distribution across the line. From this LSF, the beam width can be determined using the same conventions applied for the PSF, either at FWHM level or at the $1/\mathrm{e}^2$ level of its maximum value.

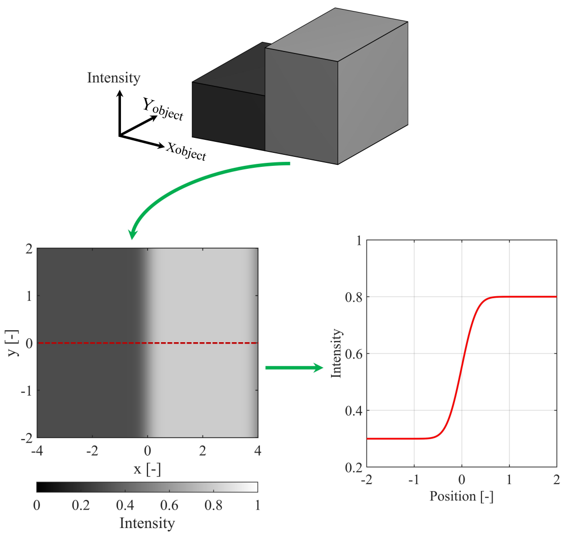

Figure 3. An edge in the object space (top), its corresponding blurred image (bottom left), and the resulting ESF (bottom right).

To estimate the LSF, a perfect line is required; however, in practice, this condition can only be approximated by neglecting the line thickness and assuming a defined beam shape (Lichti and Jamtsho, 2006). Therefore, the LSF is commonly derived from the system's response to an edge, described by the edge spread function (ESF).

As shown in Figure 3, when an edge in the object space is recorded by an optical system, the blurring of the edge image is due to the system's ability to resolve the edge. The variation of the intensity values in the direction perpendicular to the blurred edge represents the ESF. In the case of a perfect optical system, the ESF would produce a sharp step transition (Delakis et al., 2009). However, due to the imperfections of the optical system, the ESF appears as a gradual transition. By differentiating the ESF with respect to the direction normal to the edge using

$$\mathrm{LSF}(x) = \frac{d}{dx}\left(\mathrm{ESF}(x)\right), \tag{2}$$

the LSF can be obtained (Boreman, 2021). Finally, the beam width can be estimated from the derived LSF at FWHM or at the $1/\mathrm{e}^2$ level.

3.2 Estimation of the effective laser beam footprint

The proposed workflow for estimating the effective laser beam footprint, adapted from the concepts of the ESF and LSF, consists of five steps 1) to 5). It is illustrated in Figure 4 and explained in the following.

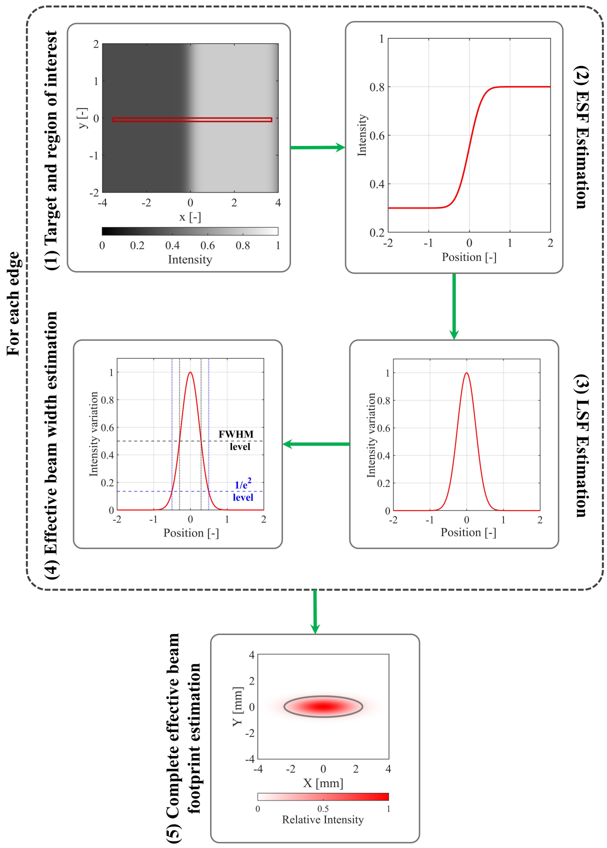

Figure 4. Workflow for estimating the effective beam footprint using the ESF-LSF approach: From the target cross section (1) to ESF estimation (2), LSF estimation (3), effective beam width estimation (4) and the effective beam footprint (5).

1) Target and region of interest The process begins with selecting a suitable target that provides a distinct edge transition based on the intensity values of the point cloud. In addition, the target should contain edges oriented in different directions so that the beam width can be estimated for each direction, thereby defining the locus of the effective laser beam footprint.

For each edge, a region of interest (ROI) is defined perpendicular to the edge. This ROI acts as a cross section within the point cloud of the target along that edge. The data within the ROI are represented by the relationship between the distance of each point, measured from the first point in the ROI, and its corresponding intensity value.

2) ESF estimation Subsequently, a step function I(x) can be fitted through these data points. In this study, a four-parameter logistic function is used:

$$I(x) = \mathrm{d} + \frac{\mathrm{c} - \mathrm{d}}{1 + \exp[-\mathrm{k}(x - \mathrm{x_0})]}, \tag{3}$$

with $I(x)$ = intensity variation across the edge, x = position of the point within the cross section, c = upper asymptote corresponding to the maximum intensity, d = lower asymptote corresponding to the minimum intensity, $\mathrm{x_0}$ = inflection point defining the midpoint of the transition, k = slope parameter controlling the sharpness of the edge transition.

As the ESF can be described as the convolution of an ideal step edge with a Gaussian impulse response, which has no closed-form expression, the four-parameter logistic function is therefore used as a practical closed-form alternative. By estimating the four parameters c, d, $\mathrm{x_0}$, and k using a least-squares approach, the ESF corresponding to this edge is obtained.

3) LSF estimation By differentiating the fitted ESF in Eq.(3), the corresponding LSF can be derived, describing the variation of intensity in the direction perpendicular to the edge and enabling the estimation of the beam width:

$$\frac{\mathrm{d}I(x)}{\mathrm{d}x} = (\mathrm{c} - \mathrm{d})\,\mathrm{k}\,\frac{\exp[-\mathrm{k}(x - \mathrm{x_0})]}{(1 + \exp[-\mathrm{k}(x - \mathrm{x_0})])^2}. \tag{4}$$

4) Effective beam width estimation The beam width can be quantified either at FWHM ($\mathrm{W_{FWHM}}$), as in

$$\mathrm{W_{FWHM}} = x_{\mathrm{right}}(50\%\,\mathrm{LSF}) - x_{\mathrm{left}}(50\%\,\mathrm{LSF}), \tag{5}$$

where

$$x_{\mathrm{right}}(50\%\,\mathrm{LSF}) = \mathrm{x_0} - \frac{1}{\mathrm{k}}\ln(3 - 2\sqrt{2}),$$
$$x_{\mathrm{left}}(50\%\,\mathrm{LSF}) = \mathrm{x_0} - \frac{1}{\mathrm{k}}\ln(3 + 2\sqrt{2}),$$

or at the $1/\mathrm{e}^2$ level ($\mathrm{W}_{1/\mathrm{e}^2}$), as in

$$\mathrm{W}_{1/\mathrm{e}^2} = x_{\mathrm{right}}(1/\mathrm{e}^2\,\mathrm{LSF}) - x_{\mathrm{left}}(1/\mathrm{e}^2\,\mathrm{LSF}), \tag{6}$$

where

$$x_{\mathrm{right}}(1/\mathrm{e}^2\,\mathrm{LSF}) = \mathrm{x_0} - \frac{1}{\mathrm{k}}\ln\left(\frac{4 - 2/\mathrm{e}^2 - 4\sqrt{1 - 1/\mathrm{e}^2}}{2/\mathrm{e}^2}\right),$$

$$x_{\mathrm{left}}(1/\mathrm{e}^2\,\mathrm{LSF}) = \mathrm{x_0} - \frac{1}{\mathrm{k}}\ln\left(\frac{4 - 2/\mathrm{e}^2 + 4\sqrt{1 - 1/\mathrm{e}^2}}{2/\mathrm{e}^2}\right),$$

in which x_{left} = position on the left side of the LSF curve at the specified level and x_{right} = position on the right side of the LSF curve at the specified level. Therefore, this approach enables an intensity based estimation of the effective beam width in the direction perpendicular to the edge.

5) Complete effective beam footprint estimation The estimated one-dimensional effective laser beam width covers the direction perpendicular to the transition area only. Thus, the effective beam width can be estimated for various edges in different orientations. Consequently, the effective beam width values obtained from all edges are fitted to a geometric form that represents the underlying footprint best. The complexity of this geometric form can principally be adapted to the variability of the estimated beam widths.

In case of our present investigations, the footprint can be approximated quite well by an ellipse. From this ellipse, the semi-major and semi-minor axes (a, b) as well as the orientation angle β can be estimated, allowing the effective beam footprint to be characterized.

4. Experiment

In order to implement the workflow described in Section 3.2, this section presents the experimental setup, including the target design, scanner configuration, and measurement arrangement. The study investigates the Z+F Imager 5016A (Zoller + Fröhlich GmbH, 2025) as it provides raw intensity values which are used to estimate the effective laser beam width.

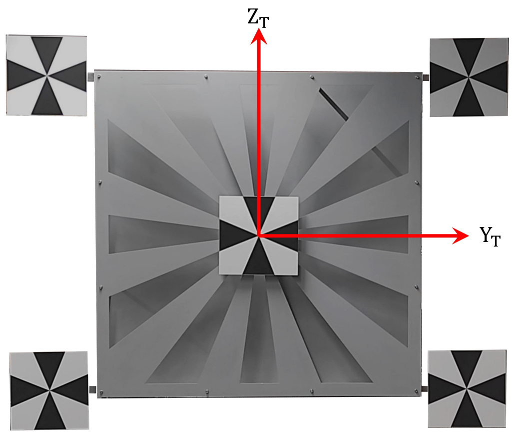

Figure 5. Test specimen used for estimating the effective beam width, with the BOTA8 target positioned at the center and four additional targets for registration. The realized target coordinate reference system is illustrated in red.

As it is essential to use a target that provides distinct intensity transition edges, the BOTA8 target represents a suitable choice for this experiment. The target, originally proposed by Janßen et al. (2019), has dimensions of 30 × 30 cm and features an eight-fold pattern composed of four white and four black areas, forming eight high-contrast transition edges. For this setup, the BOTA8 target was mounted at the center of the Böhler-star target (Böhler et al., 2003; Schmitz et al., 2020), which served as a stable holder, as illustrated in Figure 5. In addition, four auxiliary targets were positioned at the outer edges and used for the later registration of the scans.

Before scanning the target, a reference coordinate system was established. This system was defined with the center of the BOTA8 target as the origin and was constructed using a Leica Nova TS60 (Leica Geosystems AG, 2025) total station. The Y-axis (Y_T) runs laterally along the target plane, the Z-axis (Z_T) runs vertically upward, and the X-axis (X_T) is oriented normal to the target surface, forming a right-handed coordinate system (Figure 5). After defining the reference frame, the centers of the four auxiliary targets were measured within the same system. To ensure that the horizontal planes of both the target and the scanner were aligned, the vertical offset between the total station and the scanner was determined. These configurations ensure that the target lies in the Y_T-Z_T plane (Figure 5) and they ensure zero incidence angle at the target center area.

Afterwards, the scanner was positioned at two distances, 10 m and 20 m, from the target. To minimize potential measurement drifts caused by thermal fluctuations within the instrument, the scanner was allowed to warm up prior to data acquisition (Janßen et al., 2020). At each distance, two scanning configurations were applied, with scanning rates of 546.495 kHz and 1092.99 kHz, corresponding to mirror speeds of 13 rps and 27 rps, respectively. Both configurations provided a point spacing of 1.6 mm at 10 m (Zoller + Fröhlich GmbH, 2025), allowing the evaluation of the effect of varying the scanning rate and mirror rotation speed. To assess the robustness of the proposed workflow, 50 scans were acquired for each distance and scanning configuration.

Using the centroid estimation algorithm proposed by Janßen et al. (2019), all scans were geo-referenced based on the estimated target centers and the known target coordinates within the target coordinate system. The registration was performed in the Z+F LaserControl software (Zoller + Fröhlich GmbH, 2021) provided by the manufacturer. Consequently, in all scans, the target center corresponds to the origin of the coordinate system, and the axis orientation remains identical to that of the target reference frame. This enables direct comparison between different distances and scanning configurations.

For the analysis of the transition areas, the ROIs were constructed at each edge of the eight-fold pattern of the BOTA8 target, all eight ROIs were placed 5 cm from the target center (Figure 6). The length of each ROI was defined according to its distance from the center; in this configuration, each ROI had a length of 5 cm and a thickness of 5 mm. All ROIs were oriented perpendicular to their respective edges to capture the intensity variation across the transition areas. After segmenting the point cloud within each ROI, the data points were projected along the corresponding ROI direction to ensure that all estimations were consistently performed along that axis.

5. Results and discussion

By applying the workflow presented in Section 3 to the experimental data described in Section 4, this section presents and discusses the obtained results. The analysis begins with the estimation of the ESF and LSF for each edge. Subsequently,

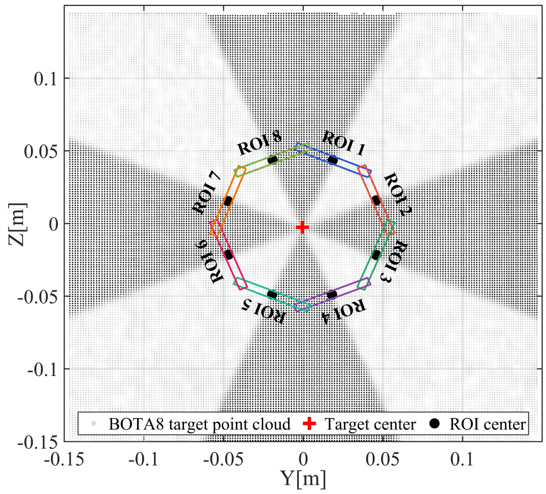

Figure 6. The BOTA8 target point cloud scanned at 10 m with a scanning rate of 546.495 kHz, showing the eight ROIs defined at an offset of 5 cm from the target center and oriented perpendicular to the eight-fold pattern edges.

the effective beam widths are determined at both the FWHM and $1/e^2$ levels for all ROIs. Finally, the fitted beam footprints corresponding to the different scanning configurations and distances are analyzed to characterize the beam's shape and orientation.

Estimation of ESF From the segmented and projected datasets at each ROI, the distances between the points were computed relative to the first point in the ROI, and their corresponding intensity values were used to derive the ESFs, as illustrated in Figure 7. To fit the ESFs, the parameters c, d, x_0, and k of the four-parameter logistic function (Eq. 3) were estimated using a least-squares adjustment for each ROI. To investigate whether the laser beam exhibits a Gaussian-like behavior, an additional Gaussian function was also fitted to the same datasets for comparison.

By examining Figure 7, it can be observed that both the four-parameter logistic function and the Gaussian function are almost identical, indicating that the laser beam of the Z+F Imager 5016A exhibits a Gaussian behavior. However, small systematic fluctuations can also be observed, mainly caused by the surface texture and the non-homogeneous painting of the target, which are particularly evident in the seventh ROI.

Estimation of LSF By differentiating the fitted ESFs using the four-parameter logistic function, and due to the rising and falling of the intensity values at the target edges, the original LSFs can be estimated. To ensure consistent visualization as well as consistent beam width estimation, the absolute values of these derivatives were used, which produced the symmetric bell-shaped curves for the eight ROIs (Figure 8).

Estimation of effective laser beam width It is noticeable that the peak widths vary among the ROIs, particularly at the second, third, sixth, and seventh ROIs, while the remaining ones appear narrower and sharper. This behavior reflects the combined influence of beam spreading, the local surface response at each edge, and the anisotropic nature of the beam. Accordingly, the effective beam width is derived from the LSF of each ROI at both the FWHM and the $1/e^2$ levels.

Estimation of complete effective laser beam footprint Based on the estimated values of the effective beam widths, the

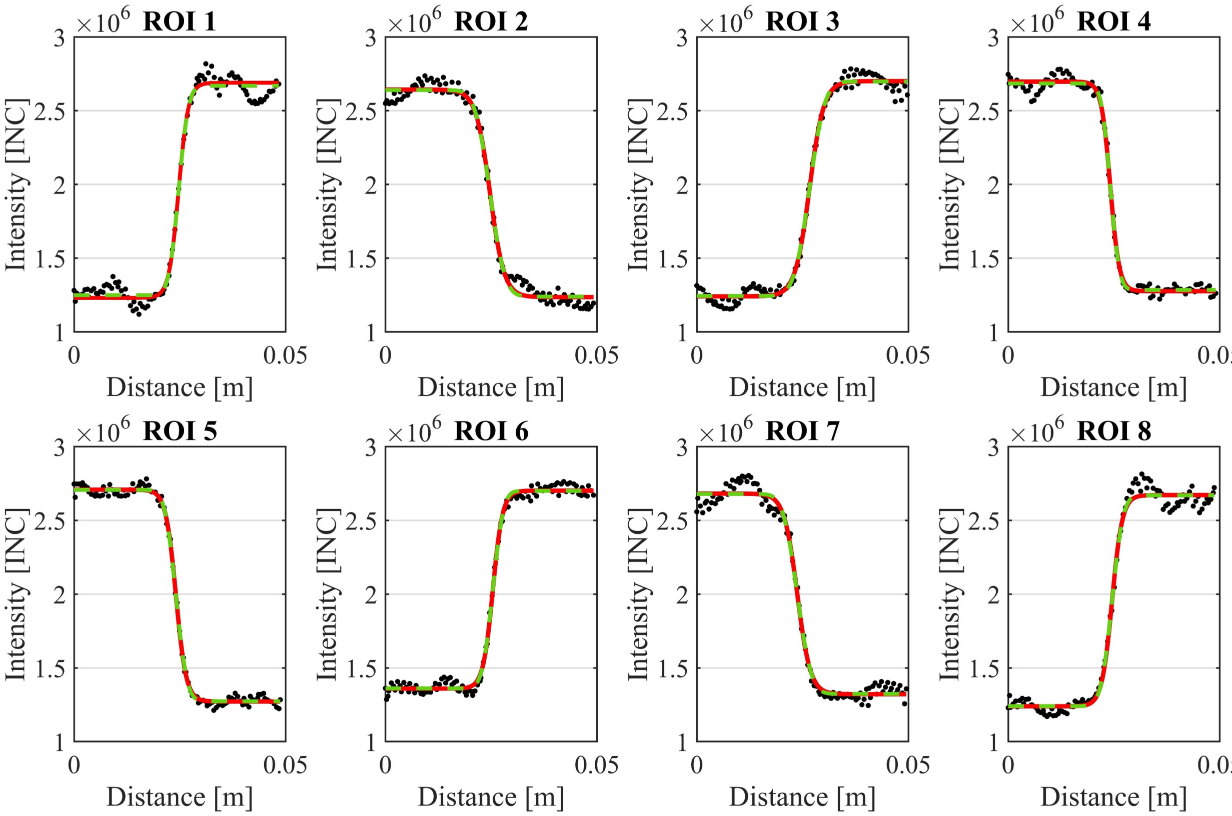

Figure 7. The ESFs derived at the eight ROIs of the BOTA8 target scanned with a scanning rate of 546.495kHz at a distance of 10 m. The black dots represent the ROI datasets after segmentation and projection, while the red and green curves correspond to the fitted four-parameter logistic and Gaussian functions, respectively.

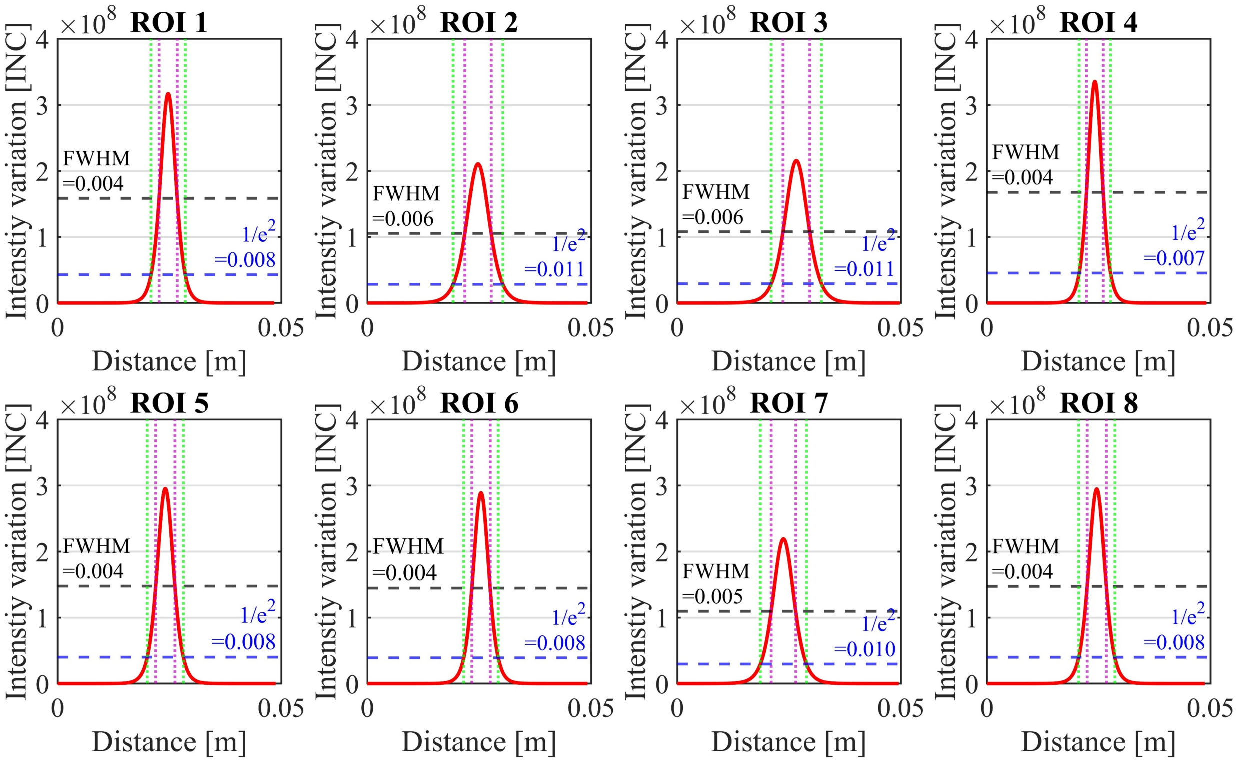

Figure 8. The absolute LSFs derived at the eight ROIs of the BOTA8 target scanned with a rate of 546.495 kHz at a distance of 10 m. The effective beam widths are shown at the FWHM (dashed black) and $1/e^2$ (dashed blue) levels, with their corresponding x_{left} and x_{right} positions indicated by dotted magenta and green lines, respectively.

locus of the effective laser beam footprint can be determined by fitting an ellipse through the estimated effective beam widths at the eight ROIs. Figures 9 and 10 show the effective laser beam footprints for the two scanning rates used to scan the target, as described in Section 4, at distances of 10 m and 20 m. The footprints were obtained after averaging the effective beam widths at the FWHM level for each ROI from 50 scans, together with the corresponding standard deviation (STD) of the beam width estimation at each edge.

Table 1. Fitted beam parameters (a, b, and β) of the Z+F Imager 5016A for both 546.495 kHz and 1092.99 kHz at 10 m and 20 m distances.

Distance	**Parameter**	**Scanning rate [kHz]**	
		546.495	**1092.99**
10 m	a [mm]	5.16	5.08
	b [mm]	3.83	3.67
	β [deg]	10.6	6.7
20 m	a [mm]	8.97	9.44
	b [mm]	7.00	6.51
	β [deg]	1.4	2.6

The footprints at each distance are rotated by 90°, since the estimation of the effective beam width is performed along the direction perpendicular to the ROIs. By comparing the beam footprints at the two distances, it is evident that the footprint size increases with increasing distance for both scanning rates, which is attributed to beam divergence. Moreover, the beam footprint orientation angle β also changes with distance, as in Table 1.

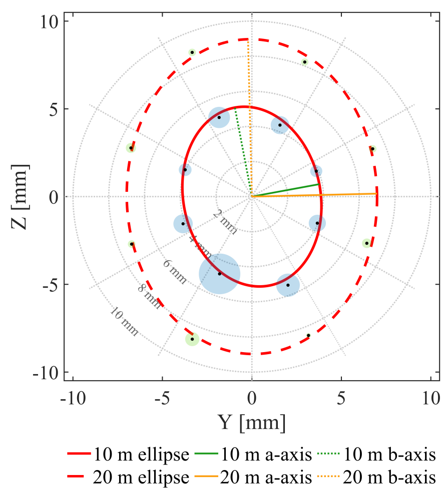

Figure 9. Estimated effective laser beam footprint at 10 m and 20 m for the 546.495 kHz scan rate, derived from the mean FWHM effective beam widths. Blue and green circles show the standard deviations at each edge, while the fitted ellipse indicates the semi-axes (a, b).

Discussion When comparing the laser footprints at the two scanning rates, they appear almost identical at 10 m. However, at 20 m, the beam width corresponding to the 1092.99 kHz configuration is slightly larger than that of 546.495 kHz. This difference can be explained by the higher mirror rotation speed at 1092.99 kHz, which increases the temporal angular resolution and reduces the integration time per sampled point. The shorter integration time affects the distribution of the received signal, leading to a slightly broader effective footprint.

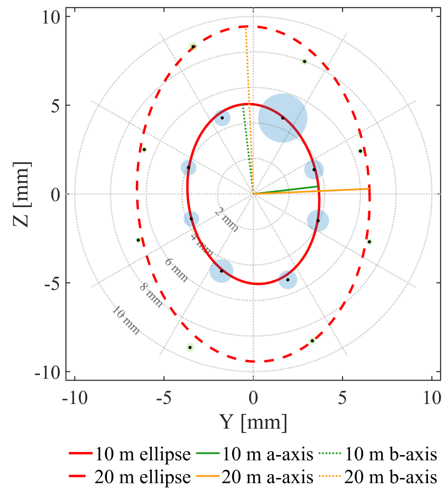

Figure 10. Estimated effective laser beam footprint at 10 m and 20 m for the 1092.99 kHz scan rate, derived from the mean FWHM effective beam widths. Blue and green circles show the standard deviations at each edge, while the fitted ellipse indicates the semi-axes (a, b).

By examining the STD values, a clear dependency on distance can be observed. At 10 m, the smaller laser footprint makes the intensity transitions within each ROI more sensitive to local surface properties, as well as to variations in the incidence angle. In contrast, at 20 m, the footprint covers a larger illuminated area, which smooths out local surface irregularities and reduces these effects, resulting in smaller STD values compared to those observed at 10 m.

6. Conclusion

This article introduces an intensity-based workflow for estimating the effective laser beam footprint by deriving the line spread function (LSF) from the edge spread function (ESF). The proposed method does not require a predefined beam model, allowing the footprint to be determined directly from the measured intensity values. The workflow was experimentally applied by scanning the BOTA8 target using the Z+F Imager 5016A at distances of 10 m and 20 m with two different scanning rates (546.495 kHz and 1092.99 kHz).

The estimated beam footprints derived from the experimental datasets show that the laser beam of the Z+F Imager 5016A exhibits a Gaussian-like behavior with an elliptical footprint at both distances. It is worth mentioning that our workflow would have been sensitive to identify footprint shapes differing from an ellipse.

As usual, the footprint size increases with increasing distance. By changing the scanning rate, the beam footprint remains nearly unchanged; however, at shorter distances, it becomes more sensitive to local surface irregularities and variations in the incidence angle. In contrast, at larger distances, the higher mirror rotation speed increases the temporal angular resolution and reduces the integration time per sampled point, leading to a broader LSF and consequently a slightly larger effective beam footprint.

Future work will focus on investigating the effect of changing the distance and target orientation on the beam footprint width and its orientation. Moreover, the workflow will be extended to estimate the resolution capability not only in the horizontal and vertical directions but also to investigate the effect of anisotropic behavior on the resolution capability. Additionally, this methodology will be applied to laser scanners that provide scaled intensity values.

Acknowledgements

This research was funded by the German Research Foundation (DFG) under grant number 490989047, DFG FOR 5455 "TLS-Defo".

References

Barbarella, M., Fiani, M., Lugli, A., 2017. Uncertainty in Terrestrial Laser Scanner Surveys of Landslides. *Remote Sensing*, 9(2).

Böhler, W., Vicent, M. B., Marbs, A., 2003. Investigating laser scanner accuracy. *The International Archives of the Photogrammetry, Remote Sensing and Spatial Information Sciences*, XXXIV, Antalya, Turkey, 696–701.

Boreman, G. D., 2021. *Modulation Transfer Function in Optical and Electro-Optical Systems*. 2nd edn, SPIE Press.

Centeno, J. A. S., Wutke, J. D., Mitishita, E. A., Vögtle, T., 2010. Two Methods to Estimate the Spot Size of Terrestrial Laser Scanners. *Journal of Surveying Engineering*, 136(3), 126–131.

Chaudhry, S., Salido-Monzú, D., Wieser, A., 2021. A Modeling Approach for Predicting the Resolution Capability in Terrestrial Laser Scanning. *Remote Sensing*, 13(4), 615.

Delakis, I., Xanthis, C., Kitney, R. I., 2009. Assessment of the limiting spatial resolution of an MRI scanner by direct analysis of the edge spread function. *Medical Physics*, 36(5), 1637–1642. https://doi.org/10.1118/1.3097633.

Goodman, J. W., 2005. *Introduction to Fourier Optics*. 3rd edn, Roberts and Company Publishers, Greenwood Village, CO.

Holst, C., Kuhlmann, H., 2016. Challenges and Present Fields of Action at Laser Scanner Based Deformation Analyses. *Journal of Applied Geodesy*, 10(1), 17–25. https://doi.org/10.1515/jag-2015-0025.

Huxhagen, U., Kern, F., Siegrist, B., 2011. Untersuchung zum auflösungsvermögen terrestrischer laserscanner mittels bÖhlerstern. *Tagungsband der DGPF (Deutsche Gesellschaft für Photogrammetrie, Fernerkundung und Geoinformation) – Fachgebiet Laserscanning und optische 3D-Messtechnik*, 31, Mainz, Germany, 409–418.

Janßen, J., Kuhlmann, H., Holst, C., 2020. Assessing the temporal stability of terrestrial laser scanners during long-term measurements. *Contributions to International Conferences on Engineering Surveying: Springer Proceedings in Earth and Environmental Sciences*, Springer, Cham, 69–84. Accessed: 2025-10-25.

Janßen, J., Medic, T., Kuhlmann, H., Holst, C., 2019. Decreasing the Uncertainty of the Target Center Estimation at Terrestrial Laser Scanning by Choosing the Best Algorithm and by Improving the Target Design. *Remote Sensing*, 11(7), 845. https://doi.org/10.3390/rs11070845.

Kerekes, G., Schwieger, V., 2021. Determining Variance-Covariance Matrices for Terrestrial Laser Scans: A Case Study of the Arch Dam Kops. A. Kopáčik, P. Kyrinovič, J. Erdélyi, R. Paar, A. Marendić (eds), *Contributions to International Conferences on Engineering Surveying*, Springer International Publishing, Cham, 57–68.

Leica Geosystems AG, 2025. Leica nova ts60 – world's most accurate total station. Available at: www.leica-geosystems.com (Accessed: 25 Oct 2025).

Lichti, D. D., Gordon, S., Tipdecho, T., 2005. Error models and propagation in directly georeferenced terrestrial laser scanner networks. *Journal of Surveying Engineering*, 131(4), 135–142.

Lichti, D. D., Jamtsho, S., 2006. Angular resolution of terrestrial laser scanners. *The Photogrammetric Record*, 21(114), 141–160.

Pesci, A., Teza, G., Bonali, E., 2011. Terrestrial Laser Scanner Resolution: Numerical Simulations and Experiments on Spatial Sampling Optimization. *Remote Sensing*, 3(1), 167–184. https://www.mdpi.com/2072-4292/3/1/167.

Schäfer, T., 2017. Berührungslose und flächenhafte Deformationsmessungen an Betonoberflächen unter besonderer Berücksichtigung der Interaktion zwischen Laserstrahl und Oberfläche. PhD thesis, Technische Universität München.

Schmitz, B., Kuhlmann, H., Holst, C., 2020. Investigating the resolution capability of terrestrial laser scanners and its impact on the effective number of measurements. *ISPRS Journal of Photogrammetry and Remote Sensing*, 159, 41–52.

Schmitz, B., Kuhlmann, H., Holst, C., 2021. Towards the empirical determination of correlations in terrestrial laser scanner range observations and the comparison of the correlation structure of different scanners. *ISPRS Journal of Photogrammetry and Remote Sensing*, 182, 228–241.

Soudarissanane, S., Lindenbergh, R., Menenti, M., Teunissen, P., 2011. Scanning geometry: Influencing factor on the quality of terrestrial laser scanning points. *ISPRS Journal of Photogrammetry and Remote Sensing*, 66(4), 389–399.

Wang, Q., Sohn, H., Cheng, J. C. P., 2016. Development of a mixed pixel filter for improved dimension estimation using AMCW laser scanner. *ISPRS Journal of Photogrammetry and Remote Sensing*, 119, 246–258.

Williams, T. L., 1999. *The Optical Transfer Function of Imaging Systems*. Institute of Physics Publishing, Bristol, UK.

Yang, Y., Holst, C., 2025. How to find geometric changes in laser scanning point clouds? A perspective on correspondence definitions. *ISPRS Annals of the Photogrammetry, Remote Sensing and Spatial Information Sciences*, X-2/W1-2025, 1003–1010.

Zhou, Y., Zhu, J., Lidu, Z., Hu, G., Xin, J., Zhang, H., Yang, J., 2024. High-Precision Monitoring Method for Bridge Deformation Measurement and Error Analysis Based on Terrestrial Laser Scanning. *Remote Sensing*, 16.

Zoller + Fröhlich GmbH, 2021. Z+f lasercontrol® software. Available at: www.zofre.de (Accessed: 25 Oct 2025).

Zoller + Fröhlich GmbH, 2025. Z+f imager® 5016a. Available at: www.zofre.de (Accessed: 8 Feb 2025).